Supplementary material

Waste PET upcycling to conductive carbon-based composite through laser-assisted carbonization of UiO-66

Dmitry Kogolev[‡a], Oleg Semyonov[‡a], Nadezhda Metalnikova[a], Maxim Fatkullin[a], Raul D. Rodriguez[a], Petr Slepicka[b], Yusuke Yamauchi[c,d], Olga Guselnikova[a,d], Rabah Boukherroub[e], Pavel S. Postnikov[*a,b]

‡ Equal contributors

a Research School of Chemistry and Applied Biomedical Sciences, Tomsk Polytechnic University, Tomsk 6340034, Russian Federation, postnikov@tpu.ru

b Department of Solid State Engineering, University of Chemistry and Technology, 16628 Prague, Czech Republic

c Australian Institute for Bioengineering and Nanotechnology (AIBN), The University of Queensland, Brisbane, QLD 4072, Australia

d JST-ERATO Yamauchi Materials Space-Tectonics Project and International Center for Materials Nanoarchitectonics (WPI-MANA), National Institute for Materials Science (NIMS), Tsukuba, Ibaraki 305-0044, Japan

e Univ. Lille, CNRS, Centrale Lille, Univ. Polytechnique Hauts-de-France, IEMN, UMR CNRS 8520, F-59000 Lille, France

Table of content

1. Materials and methods

1.1. Materials

The starting material for obtaining a hybrid material with conductive properties were transparent sheets of polyethylene terephthalate (PET) made from recycled plastic and purchased in hardware stores in the city of Tomsk, Russia. All reagents and solvents were purchased from Sigma-Aldrich and used without prior purification.

Preparation of PET@UiO-66 under solvo-thermal conditions

PET@UiO-66 was prepared according to the adapted procedure reported before [1]. In the first stage, PET sheets were prepared for hydrolysis. The PET sheet was cut into rectangles of 2 × 2.5 cm^2 in size. After that, the hydrolysis zone was marked on each rectangle. A protective polyethylene film on the PET surface was removed from this zone, and the prepared sheet was placed in a Petri dish filled with concentrated sulfuric acid. The optimization of hydrolysis conditions is described in Section 2. After the required time, the surface-hydrolysed PET sheet was removed and washed with distilled water. It was followed by ultrasonic treatment and was dried in air overnight.

After hydrolysis, the sheet was loaded into an autoclave, where metal precursors (62.5 mg of $ZrCl_4$, 10 mL of DMF, and 0.5 mL of concentrated hydrochloric acid) were added. The mixture was kept for 10 min under constant stirring, after which 61.5 mg of terephthalic acid, prepared from waste PET bottles according to a protocol described in ref[2] was added. The autoclave was kept for 15 h at 80 °C. Subsequently, it was cooled naturally to room temperature. The resulting PET@UiO-66 material was thoroughly washed with DMF and methanol. PET@UiO-66 was activated under vacuum at 50 °C overnight.

Preparation of PET@UiO-66 by the drop-casting method

UiO-66 thin films were deposited on the PET plates by the drop-casting method. UiO-66/ethanol colloidal solution was prepared at a concentration of 30 mg/mL by sonication for 10 min at room temperature. Next, the solution was deposited on PET plates and dried under ambient conditions.

Preparation of PET@LB-UiO-66

Laser processing was conducted using a pulsed diode laser NEJE DK-8-KZ at a wavelength of 405 nm on the 1 cm^2 PET@UiO-66 area. The laser was operated at a pulse frequency of 1.6 kHz and rated power of 1500 mW. To conduct the process, the laser beam was focused on the material, and irradiation occurred when the laser moved along the plate. In our laser control system, the average power was varied by controlling the laser pulse time

and frequency. The “Laser engraving machine K4 V2.5” software allowed us to control two parameters: “*P*” (power) and “*D*” (depth). The “*P*” parameter controlled the pulse duration, while “*D*” set the pulse frequency (laser beam velocity). Optimization of the carbonization process was conducted using the Nelder–Mead method by varying parameters “*P*” and “*D*”. For carbonization of UiO-66 on the surface, the following optimized parameters were subsequently used: 49 % from nominal value (735 mW) and 26 % depth (9.0 mm s^{-1}).

1.2. Characterization of materials

Fourier-transform infrared spectroscopy (FTIR)

FTIR spectra were recorded using an Agilent Cary 630 spectrometer equipped with an attenuated total reflection (ATR) attachment. All materials were placed on a diamond crystal for further recording of spectra (resolution 2 cm^{-1} and 300 scans per spectrum). All spectra were processed using a baseline linearization in the 4000–650 cm^{-1} region.

X-ray powder diffraction (XRPD)

The crystal structure of the samples was studied by X-ray diffraction using an XRD-7000S instrument (Shimadzu, Japan) in the scanning range of 3–70°. X-ray diffraction patterns were recorded using a CuKα tube (30 mA, 40 kV, and 1 nm slit) in the Bragg–Brentano configuration.

Scanning electron microscopy with energy dispersive X-ray analysis (SEM-EDX)

The images were taken on a Tescan MIRA 3 LMU instrument in the reflected electron diffraction mode. The instrument was equipped with an Oxford Instrument Ultim Max 40 energy-dispersive X-ray device. All samples were coated with a carbon layer by magnetron sputtering. Scanning was performed using an accelerating voltage of 10 kV. Before direct imaging, the samples for cross sections were prepared by freezing in liquid nitrogen and subsequently cutting with scissors.

X-ray photoelectron spectroscopy (XPS)

The XPS spectra were recorded on a Thermo Fisher Scientific XPS NEXSA spectrometer equipped with an Al K Alpha X-ray monochromatic emitter with an energy of 1486.6 eV. Survey spectra were recorded using radiation with an energy of 200 eV and an energy resolution of 1 eV. High-resolution spectra were collected using radiation with an energy of 50 eV and a resolution of 0.1 eV. The analysis area was 200 μm^2. A flood gun was used to compensate for the charges. A monatomic gun was used for depth profiling with an energy of 4000 eV.

Ultraviolet–visible spectroscopy (UV-vis)

Diffuse reflectance spectra were recorded on pure material samples on an Analytik Jena SPECORD250+ spectrometer equipped with an integrating sphere. Polytetrafluoroethylene was used as a reference.

Raman spectroscopy

For the analysis of the chemical composition of the samples, Raman spectra were acquired using a Renishaw inVia Raman microscope with a green laser source (532 nm). The laser beam was focused on the sample using a 10× objective (spectrum accumulations

number–10, exposure time–20).

Band gap calculation

The band gap energies (E_g) of the PET@UiO-66 and PET@LB-UiO-66 materials were determined using the Tauc equation at the point of intersection of the approximate tangent to the linear part of the Tauc plots with the abscissa axis:

$$\alpha \times h \times v = A \times (h \times v - E_g)^{n/2}. \quad (1)$$

Here α, h, v, A, E_g represent the molar absorptivity, Planck's constant, light frequency, absorption and band gap energy, respectively. The value of n for a semiconductor is determined by the type of junction (n = 4 for a direct junction and n = 1 for an indirect junction).

The four-point probe technique

MS Tech MST 4000A microprobe station was used to arrange the tips in a square with a constant distance of 450 μm in between.

Sheet resistance calculation

Sheet resistance (R_{sh}) of the PET@LB-UiO-66 materials was determined using the four-point probe technique in a square configuration according to the equation (2):

$$R_{sh} = (2 \times \pi / \ln 2) \times (V/I), \quad (2)$$

where V and I correspond to applied voltage and current, respectively.

Inductively coupled plasma mass spectrometry (ICP-MS)

Zr content of the PET@UiO-66 and PET@LB-UiO-66 were measured by an inductively coupled plasma mass spectrometer (ICP-MS, Agilent 7500cx, Agilent Technologies, USA).

CHNS elemental analysis

C and H content of the PET@UiO-66 and PET@LB-UiO-66 were determined by an elemental composition analyzer (EuroEA 3000, Eurovector Instruments, Italy).

Contact angle (CA) measurements (Wettability)

Water CAs were measured by the Drop Shape Analyzer System (DSA100, Kruss, Germany) at seven positions (drop volume = 2 μL) at room temperature.

Optical images

Optical images were taken using Leica S9i microscope.

Profilometry

Surface topography images were recorded in the noncontact mode with a MicroXAM-100 interference profilometer (KLA Tencor).

Mechanical test

The abrasion test was performed on a PET@LB-UiO-66 for the mechanical resilience

estimation. During the abrasion test, PET@LB-UiO-66 (5 × 5 mm) was placed in the rotating (100 rpm) container 3/4 filled with abrasive sand (0.5 mm in diameter) for 24 h, as shown schematically in Figure S15.

Solvent resistance test

PET@LB-UiO-66 samples were soaked in toluene, chloroform, dichloromethane, ethanol, distilled water, and acetone for 6 hours prior to washing by MeOH and drying. The sheet resistance of treated material was measured by four-point probe technique. As additional evidence of morphological changes, the optical images were taken by Leica S9i microscope.

Photothermal measurements

Photothermal performance was characterized by 455, 530, 660, 780, and 1050 nm LED (Thorlabs) in closed black camera. A thermal image was recorded using a 60 × 60 pixel camera HT-02 from Hit (China) operating at a 13 cm distance from the sample.

2. Optimization of PET hydrolysis

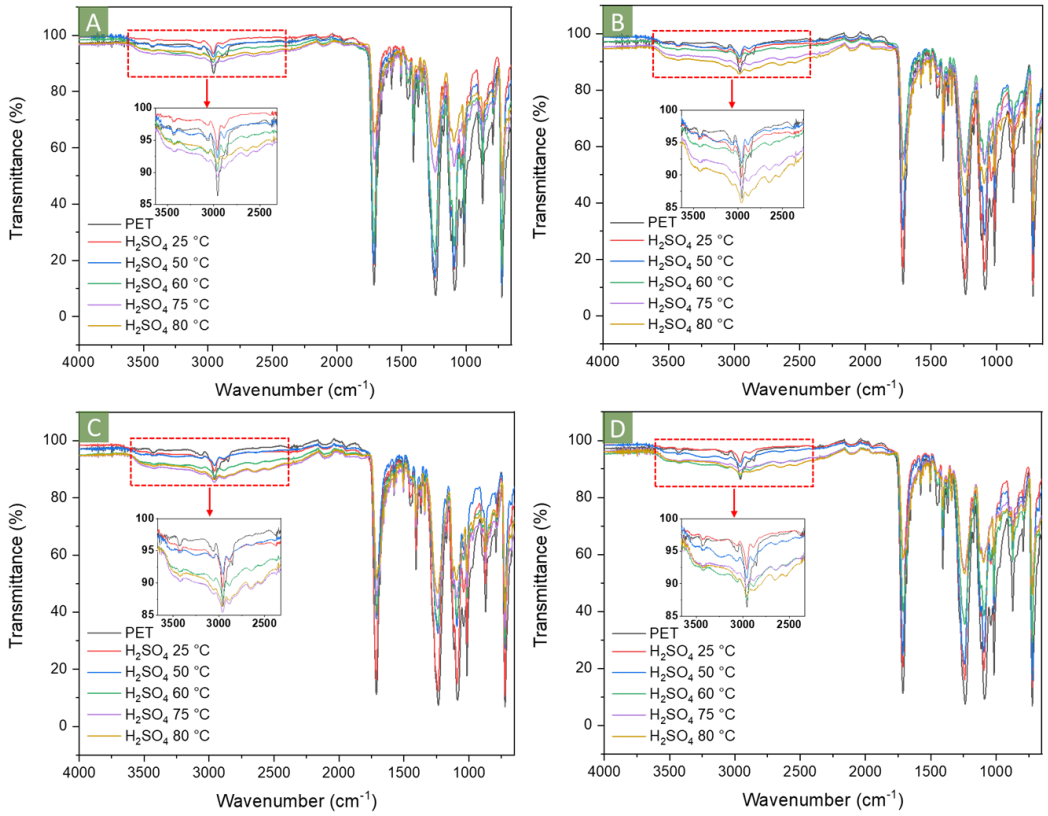

Fig. S1. FTIR spectra of pristine and hydrolysed PET (PET-H) plates using concentrated H_2SO_4 for (A) 1, (B) 2.5, (C) 5, and (D) 10 mins.

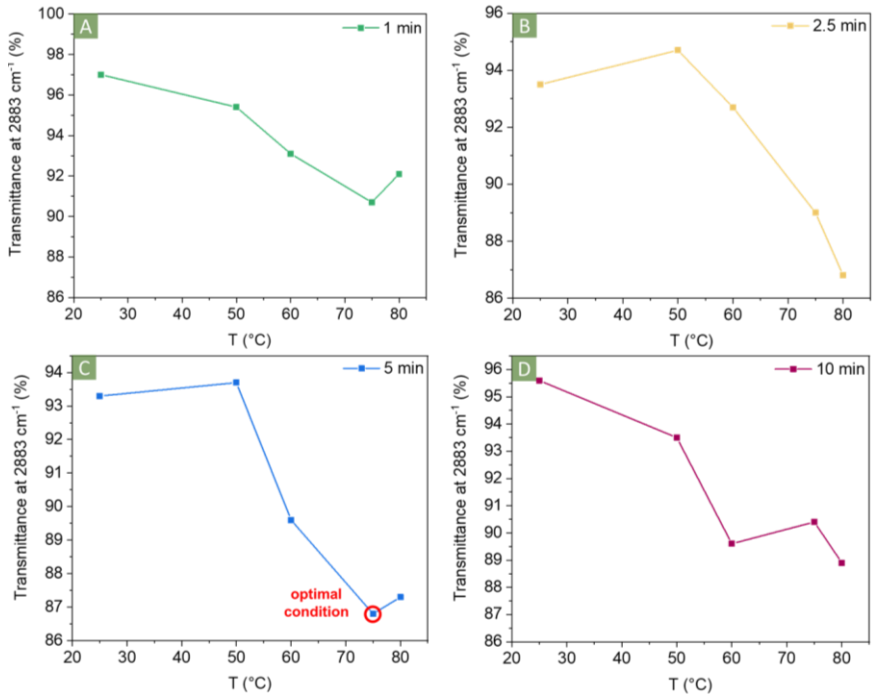

Fig. S2. Dependence of transmittance at 2883 cm^{-1} (O-H vibration stretching band) on different hydrolysis temperatures (25–80 °C) and times (1, 2.5, 5, and 10 min).

Optimization was conducted by varying the temperature (25, 50, 60, 75, and 80 °C) and the hydrolysis time (1, 2.5, 5, and 10 min) (Fig. S1,2). The highest used temperature was 80 °C because further increase of the temperature would have caused material embrittlement. Optimal parameters were chosen based on the stretching vibrations of the O-H bond intensity in the FTIR spectra of PET-H.

For optimization, we tested different hydrolysis times (1, 2.5, 5, and 10 min). After 1 min of hydrolysis, the OH-related peak was weak. However, prolonged time increased the transmittance at 2883 cm^{-1}. The most intensive peak was registered after 5 min of hydrolysis at 75 °C. Approximately equal intensity was observed at 80 °C; however, this condition led to the embrittlement of the film. Prolonging the time to 10 min did not increase the OH-related peak intensity. Therefore, 5 min of hydrolysis at 75 °C was chosen as the optimal parameter.

3. PET@UiO-66 synthesis

Surface metal-organic framework (SurMOF) synthesis was performed using a solvo-thermal reaction adopted from[3].

The successful formation of UiO-66 on PET surface was confirmed by FTIR analysis. The FTIR spectrum of PET@UiO-66 exhibited the characteristic signals of PET at 1714 cm^{-1} and UiO-66 at 1584 cm^{-1} and 1397 cm^{-1} due to asymmetric and symmetric stretches of COO-Zr bonds (Fig. S3A)[4]. XRD pattern of PET@UiO-66 revealed typical UiO-66 related diffraction peaks at 7.6° and 8.6°. They were absent in pristine and hydrolysed PETs and matched well with the simulated pattern based on the single crystal structure of UiO-66 from ICDD database (Fig. S3B)[5]. Besides, the appearance of an absorption peak at 375 nm, in contrast to pristine and PET-H, was observed in the UV-vis spectrum of PET@UiO-66 (Fig. S3C).

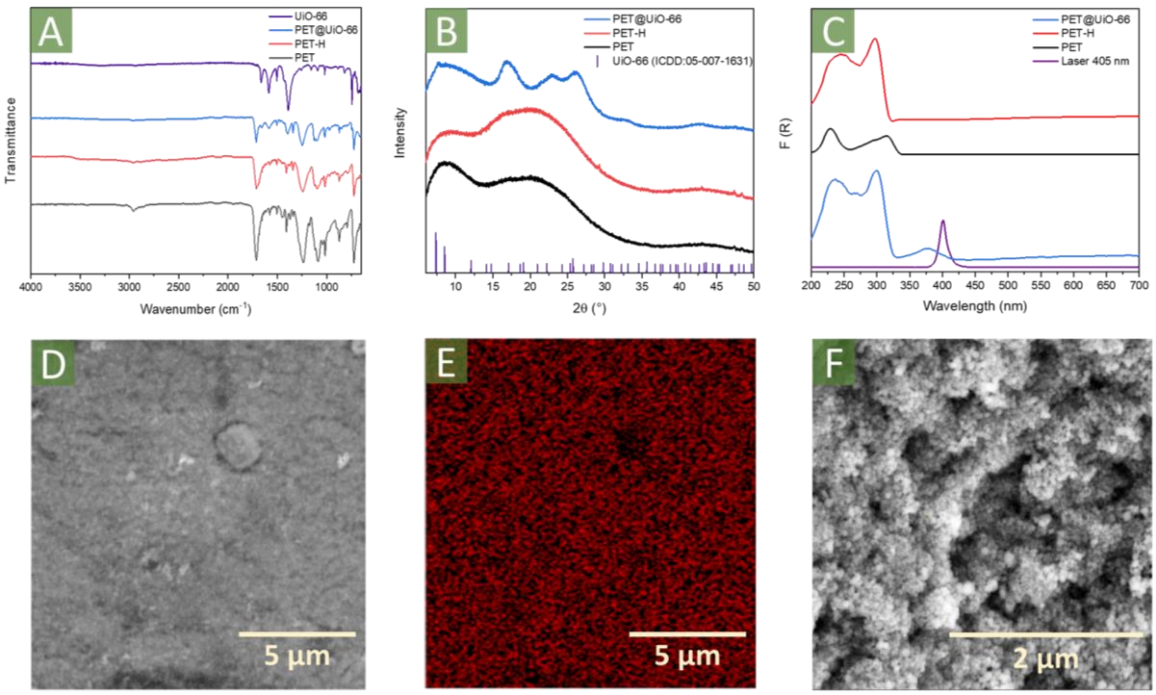

Fig. S3. Characterization of PET@UiO-66: (A) FTIR spectra, (B) XRD patterns, (C) UV- vis spectra, and (D, E) SEM-EDX map of Zr. (F) SEM image at higher magnification.

The surface morphology of PET@UiO-66 and element distribution of UiO-66 across the surface was investigated by SEM-EDX technique (Fig. S3D-F). After the surface-assisted growth of UiO-66, the initial structure was covered by UiO-66 crystallites (Fig. S3F). The MOFs layer was represented by aggregated polyhedral-shape nanoparticles, approximately 50–100 nm in size, which is consistent with previously published results[6]. The EDX mapping

demonstrated the homogeneous Zr distribution with a relatively high Zr concentration of approximately 16.6 wt.% (Fig. S3D,E). XPS spectroscopy was applied to investigate the chemical state of the PET@UiO-66 surface (Fig. S4). The UiO-66 growth was evidenced by the presence of approximately 1 % Zr on the PET surface. SurMOF synthesis also led to the appearance of the Zr-O component in the O 1s region (Fig. S4C). The binding energies of Zr 3d peaks of PET@UiO-66 at 182.9 and 185.2 eV are in a good agreement with reported data (Fig. S4D)[6].

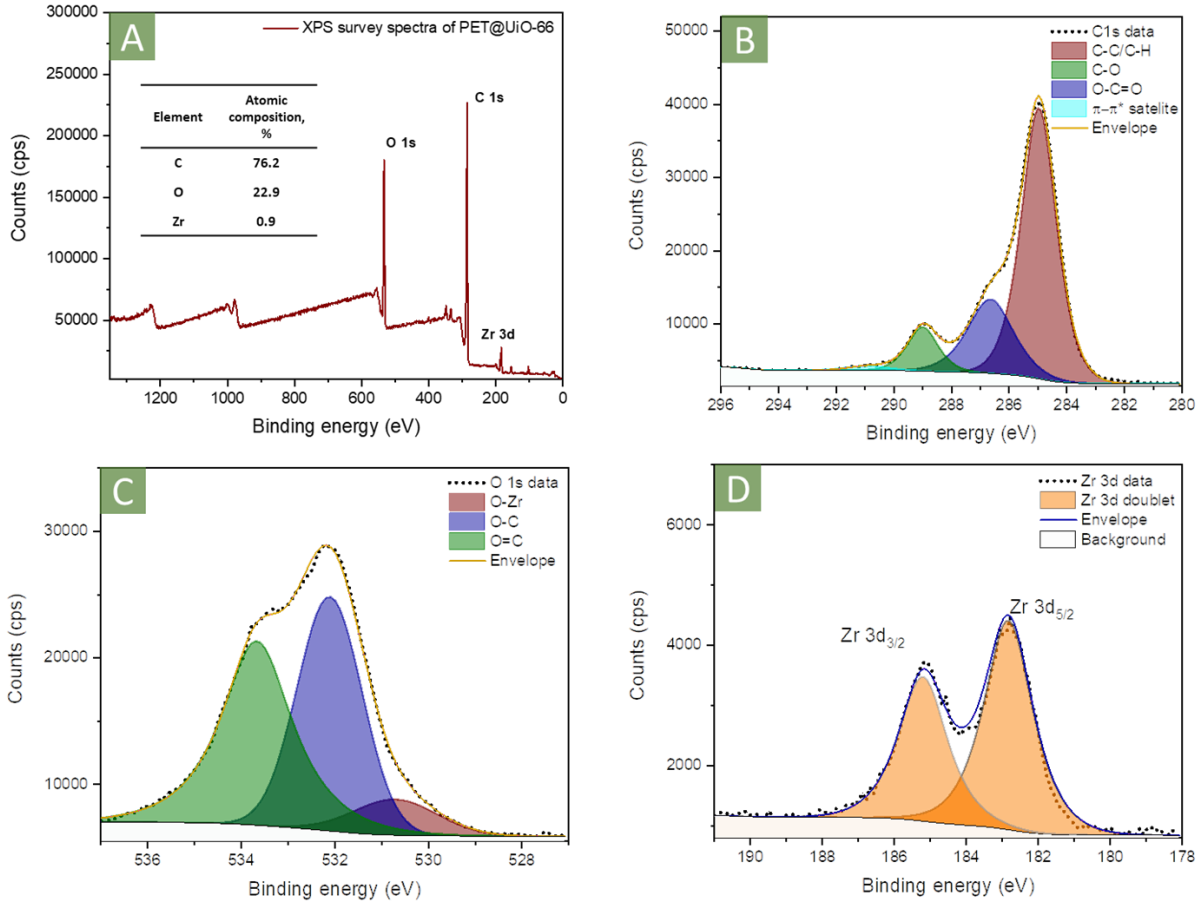

Fig. S4. Characterization of PET@UiO-66 by XPS: (A) survey spectrum, (B) C 1s, (C) O 1s, and (D) Zr 3d regions.

4. Scribing optimization

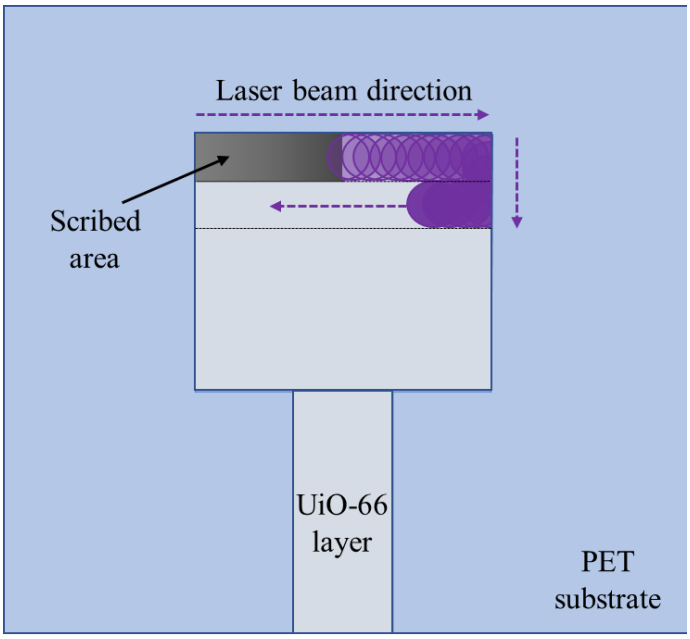

Fig. S5. Schematic illustration of the path of UiO-66 laser scribing process.

The Nelder–Mead method is a reliable technique for the optimization of functions containing several variables. It is a simple and effective method to optimize functions without using gradients. At the first stage, the simplex is created from *n+1* number of tops. Next, the values of the optimized functions are estimated. Next, a successive simplex, which reflects the worst point relative to the centre of gravity, is created. The values of the function on the vertex of the simplex are determined again. Thus, the operation of reflecting a bad point is repeated creating a new simplex. Depending on the values of the optimized function and desire of the experimenter, the operations of contraction, expansion, and shrinkage can be conducted. Optimization continues until the desired value of the function (sheet resistance of the sample) is reached or till optimization is expediated (*n+1* successive simplexes without improving the result).

Optimization was conducted by the Nelder-Mead algorithm. The chosen variables were: power (mW) and laser beam speed (mm s^{-1}). Termination criterion is a sheet resistance of the sample or (*n+1*) successive simplexes without improving the result (*n* is the number of variables). The optimization was conducted to minimize the sheet resistance of the sample.

Table S1. Table of parameters for Nelder–Mead optimization

Point	Laser power*, mW	Laser speed, mm s^{-1}	Sheet resistance, Ω/square
1	600	9.9	23.4 ± 1.3
2	750	9.9	23.7 ± 11.8
3	600	8.3	Non-conductive
4	750	12.4	Non-conductive
5	713	11.0	38.7 ± 10.0
6	638	9.0	18.6 ± 2.2
7	488	9.0	78.2 ± 27.0
8	553	9.2	38.0 ± 12.4
9	690	9.7	12.9 ± 5.4
10	690	9.3	49.3 ± 10.1
11	615	9.3	67.0 ± 10.4
12	630	9.5	39.9 ± 8.0
13	810	8.3	17.7 ± 2.2
14	705	9.0	31.2 ± 5.0
15	735	9.0	10.4 ± 3.1

* Power calculated from nominal

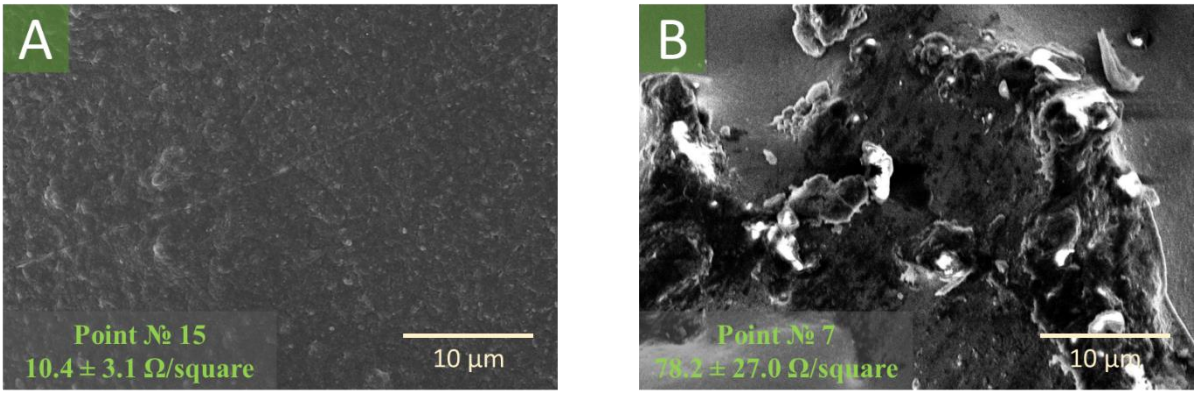

Fig. S6. SEM images of PET@UiO-66 material with (A) a close-to-perfect conductivity and (B) poor conductivity.

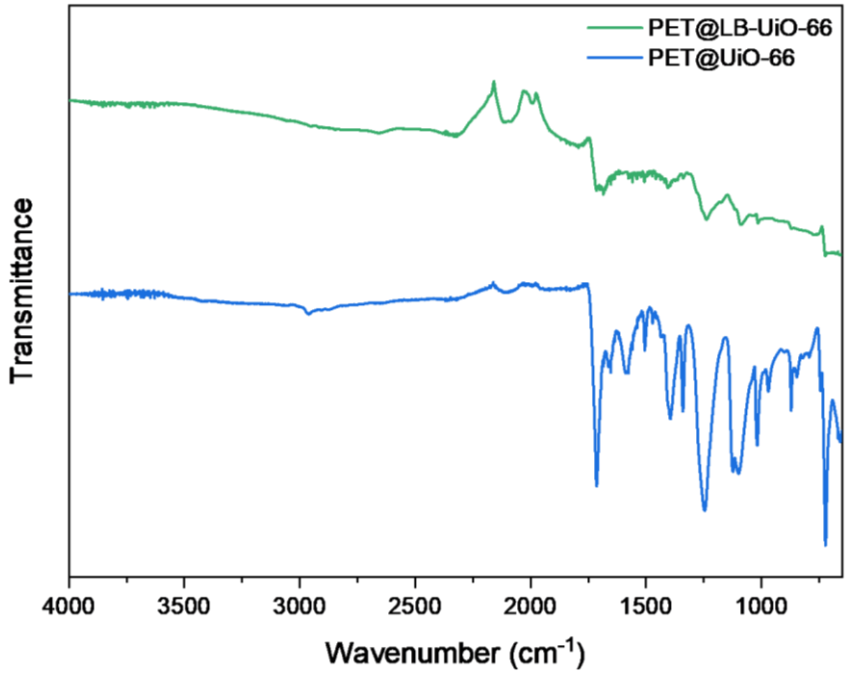

Fig. S7. FTIR spectra of PET@UiO-66 and PET@LB-UiO-66 materials.

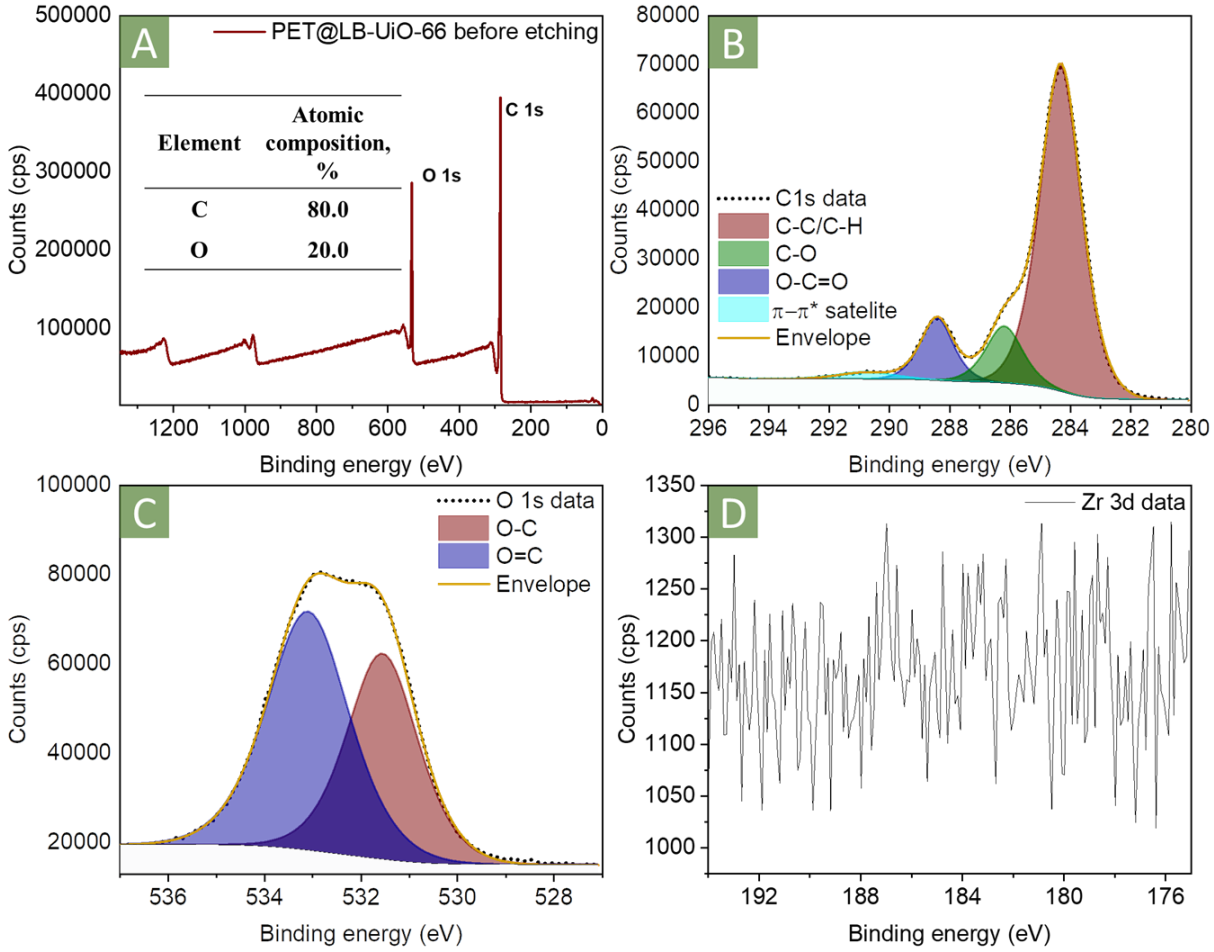

Fig. S8. XPS spectra of PET@LB-UiO-66 before Ar^+ surface etching: (A) survey, (B) C 1s, (C) O 1s, and (D) Zr 3d regions.

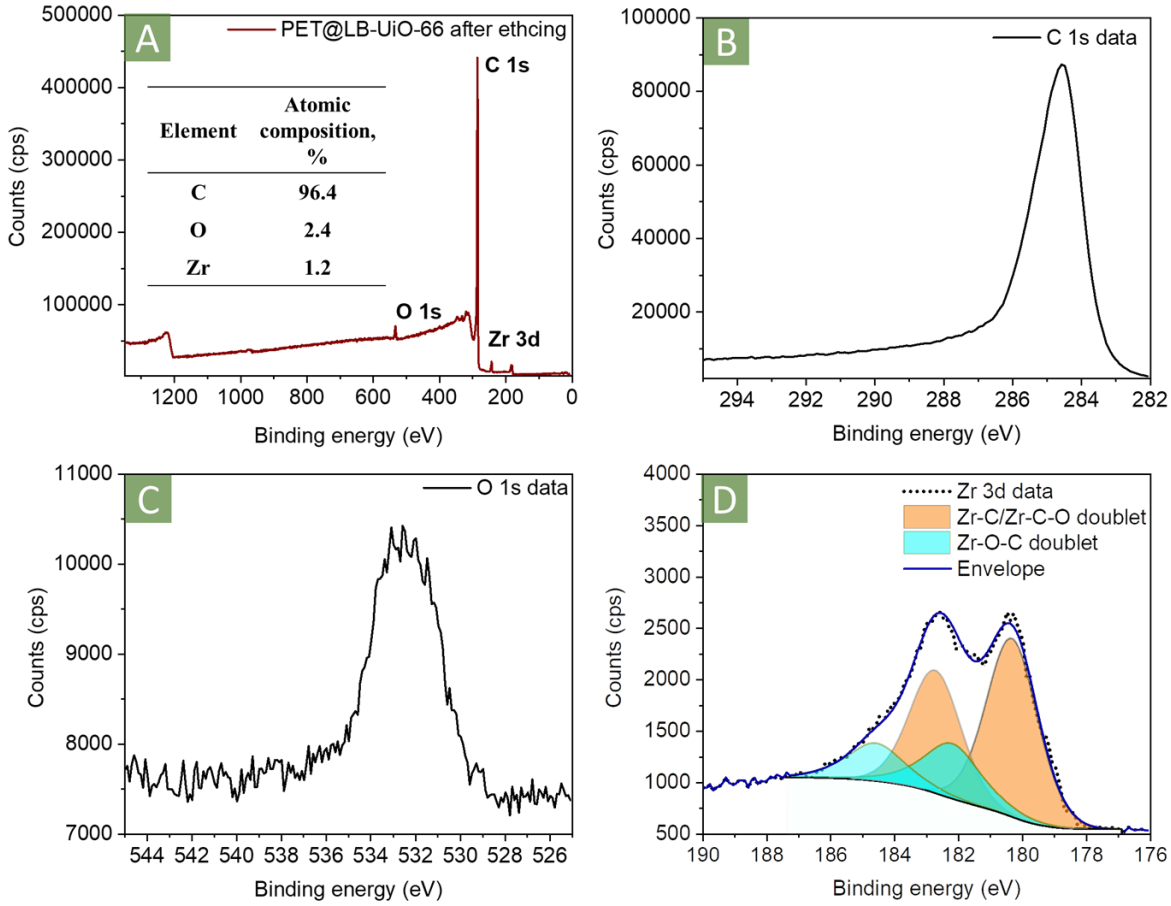

Fig. S9. XPS spectra of PET@LB-UiO-66 after Ar^+ surface etching: (A) survey, (B) C 1s, (C) O 1s, and (D) Zr 3d regions.

Table S2. Sheet resistance comparison of untreated and reduced GO and laser-induced carbonized surface materials

Materials and methods	Laser information	Applied power	Sheet resistance, Ω/square	Ref.
Unexposed GO	-	-	10^6–10^{10}	[7- 9]
Deposition of GO on a cotton fabric followed by reduction by hot press	-	-	900	[10]
Laser-reduced graphene oxide in liquid nitrogen environment	Picosecond pulsed laser: 1064 nm, pulse duration 10 ps, 100 kHz repetition rate, spot size 30 μm	-	50–60	[11]
Laser direct patterning of reduced GO on flexible (PET) substrate by femtosecond pulses	Femtosecond 515 nm laser, 280 fs pulse length, 500 kHz repetition rate	35–45 nJ pulse energy with 10–20 pulses per μm	200.0	[12]
Polyimide surface carbonization	CO_2 laser	4.5 to 8.25 W	60.0	[13]
Polyimide surface carbonization	CO_2 with 10.6 μm wavelength and a beam size of 0.127 mm	25 W	30 ± 2.6	[14]
Poly (Ph-ddm)-surface carbonization	CO_2 laser 10.6 μm, pulse frequency is 20 kHz	20 W	35.0	[15]
Laser-induced graphitization of ink based on cellulose and lignin	CO_2 laser 10.6 μm	3.3 W	3.8 ± 0.1	[16]
Carbonization of MOFs powder (LIC-(ZIF-8) and LIC-(ZIF-67))	CO_2 laser 1064 nm	4.8 W	approximately 125	[17]
Low-cost laser carbonization (PET@LB-UiO-66)	405 nm LED pulse laser	735 mW	10.4 ± 3.1	This work

Table S3. Element composition of PET@UiO-66 and PET@LB-UiO-66

Material	**CHNS, wt.%**		**ICP-MS, wt.%**
	C	*H*	*Zr*
PET@UiO-66	65.4 ± 0.4	4.9 ± 0.1	0.084
PET@LB-UiO-66	66.5 ± 0.7	5.0 ± 0.2	0.089

5. Evaluation of surface morphology changes

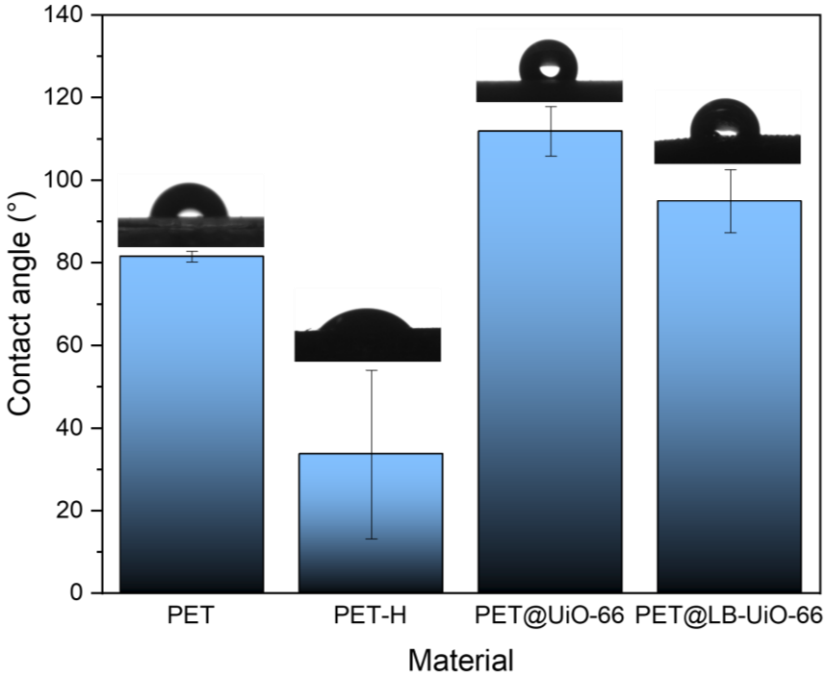

Fig. S10. Water contact angles measured on the surfaces of PET, PET-H, PET@UiO-66 and PET@LB-UiO-66.

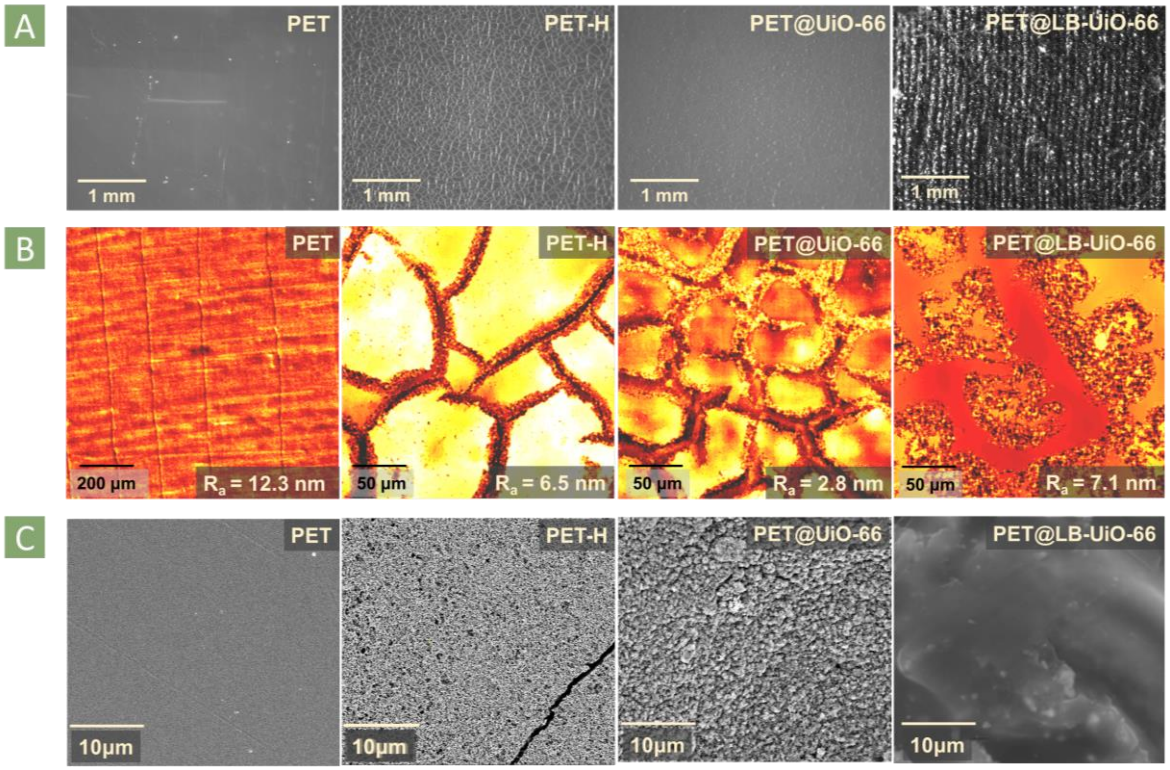

Fig. S11. (A) Optical microscope images of PET, PET-H, PET@UiO-66 and PET@LB-UiO-66. (B) Optical profilometry images of PET, PET-H, PET@UiO-66 and PET@LB-UiO-66. (C) SEM photos of PET, PET-H, PET@UiO-66 and PET@LB-UiO-66.

The changing in surface morphology during processing was indirectly analysed through WCA measurement. The initial hydrolysis of PET led to the drop of WCA (from 81.5° ± 1.3° to 33.6° ± 20.4°) due to the appearance of surface -COOH groups as well as cracks and voids. The subsequent growth of UiO-66 layer masked the surface features and blocked the -COOH groups, which can be evidenced through the increase of WCA up to 111.8° ± 6.0°. The carbonization of PET@UiO-66 formed a smooth surface with slightly decreased hydrophobicity (94.9° ± 7.6°).

The optical images confirmed the initial hypothesis about changes in surface morphology on millimetre scale (Fig. S11A). The virgin surface of PET is smooth and homogenous while hydrolysis led to the appearance of cracking networks across the whole treated surface. The growth of UiO-66 formed a homogenous microcrystalline layer, masking the cracks. Finally, subsequent carbonization led to the formation of rough and homogenous carbon layer.

Additionally, the surface morphology was characterized by optical profilometry, revealing roughness on the micrometre scale (Fig. S11B). The analysis of optical images demonstrated a trend similar to the millimetre scale: (i) the changing of smooth surface to cracked one after hydrolysis of PET (Fig. S11B); (ii) formation of microcrystalline coating, masking the cracks during growth of UiO-66 (Fig. S11B); and (iii) the appearance of new surface features after laser-scribing explained by redistribution of solid phase (carbon and ZrC) due to partial melting of PET and Marangoni effect (Fig. S11B).

Finally, we evaluated the surface morphology on microscale using SEM (Fig. S11C). Generally, SEM images revealed the formation of microporous surface of PET after hydrolysis (Fig. S11C) with cracks and voids, which turned to microcrystalline surface with homogeneously distributed UiO-66 crystallites (Fig. S11C). The carbonization of PET@UiO-66 led to the formation of a smooth composite with visible particles associated with ZrC.

6. Laser-induced graphitization of drop-casted UiO-66 on PET and pristine PET

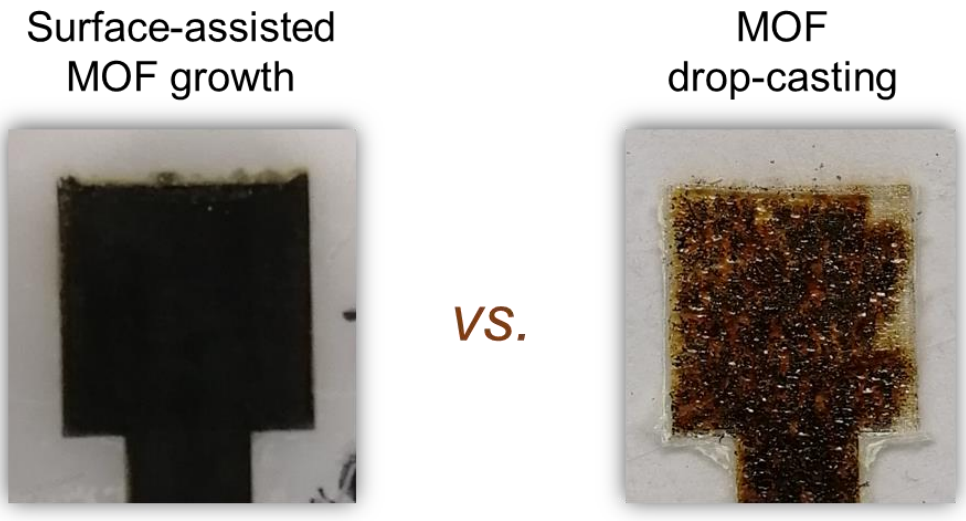

Fig. S12. Optical microscopic images of materials obtained after laser scribing: PET@LB-UiO-66 and drop-casted UiO-66.

To show the importance of covalent binding of UiO-66 layer to PET, an alternative deposition way for UiO-66 was tested. UiO-66 was suspended in EtOH and drop-casted onto PET. Laser treatment of this sample under optimized conditions (9.0 mm s^{-1} movement speed and 735 mW power) caused UiO-66 carbonization. However, the composite had no conductivity and displayed low mechanical stability of the carbon layer associated with its weak adhesion to the PET surface. When the sample was washed by water, the carbonized layer detached from PET (Fig. S12).

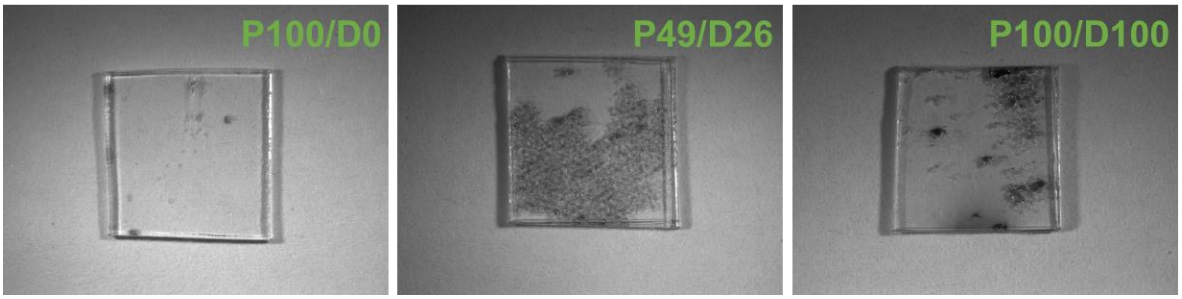

Fig. S13. Laser scribing pristine PET 1×1 cm^2 under different parameters of laser system.

7. Photothermal measurements

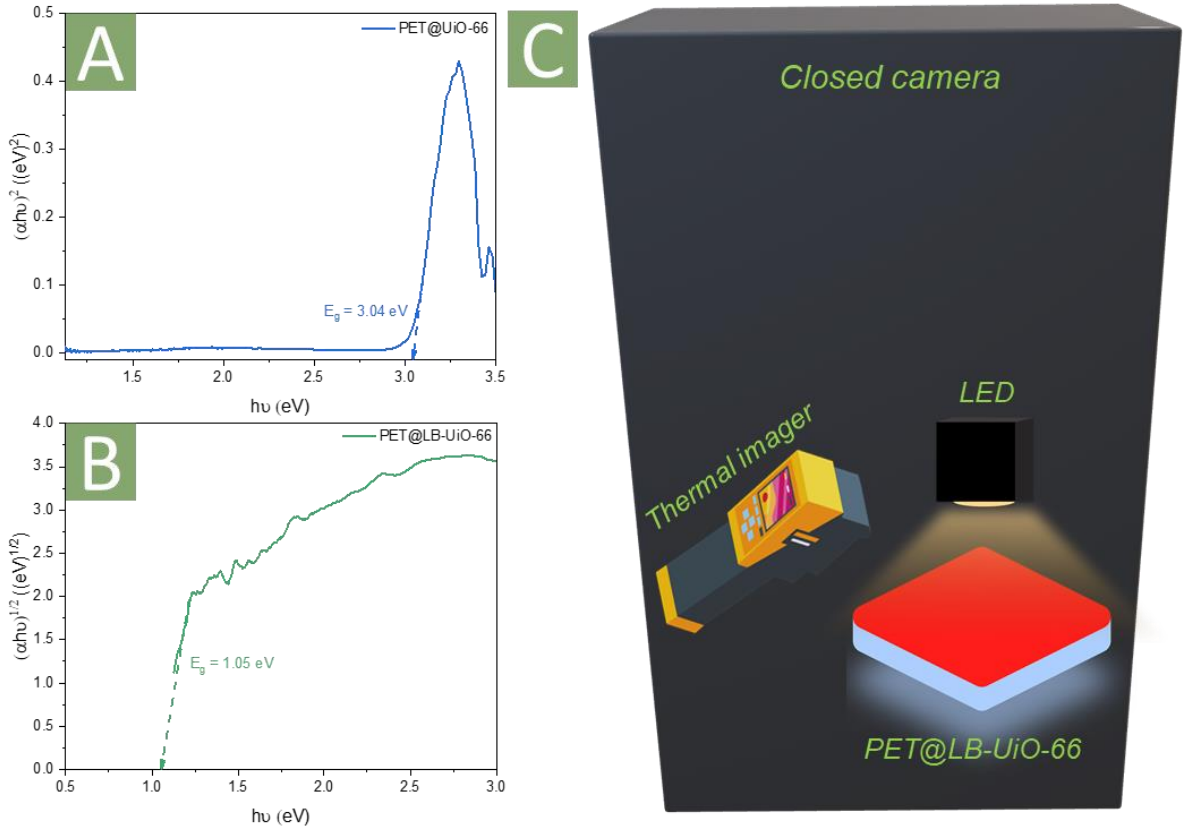

Fig. S14. Tauc plots (A) with direct band gap for PET@UiO-66 and (B) indirect band gap for PET@LB-UiO-66. (C) Schematic illustration of the photothermal measurements.

The sufficient changes in band gap are associated with the formation of graphene-like material, as reported previously for the MOFs carbonization[18–20]. Pure graphene comprises sp^2 carbon atoms and is characterized by zero band gap and high carrier mobility[21]. In graphene-based composites, zero band gap cannot be achieved due to the presence of insulating matrix. Besides graphene-like carbon, we observed the formation of zirconium carbide in our study after laser scribing. It is also characterized by a narrow band gap with low value of valence band maximum and high visible and infra-red light harvesting ability[22–24].

Table S4. Photothermal performance comparison of NPs@polymer composites, carbonized-surface materials and ZrC-polymer composites

Materials and methods	Source Information	Power density, kW/m^2	Photothermal performance, °C	Ref.
Au NPs in polypropylene fumarate	532 nm	20	51	[25]
Ti_2O_3-PVA	Solar Simulator	1	64.1	[26]
Regenerated silk fibroin/CuS fabric	1064 nm	10	Δ18.5	[27]
PVDF/Ti_3C_2 composite	Solar Simulator	1	75	[28]
Carbonized tofu	Solar Simulator	3	53.8	[29]
Surface-Carbonized Bamboos	Solar Simulator	1	52.3	[30]
Surface carbonization by CH_3SiCl_3 (10 %) gas at 60 °C: Cotton fabric Pomelo peel Polyurethane foam PET fabric	Solar Simulator	1	 53.6 71.7 59.0 50.5	[31]
ZrC(4%)-doped viscose	IR lamp (main 950 nm) 100 W, 20 cm	No data	78	[32]
Porous polypyrrole decorated polyurethane/ZrC fibrous membrane	520 nm 808 nm 980 nm	No data No data No data	73.8 89.1 85.6	[33]
ZrC particles (20 Wt%) loaded in PU membrane	Xenon lamp 300 W	No data	70.5	[34]
ZrC and graphene-like carbon structure	LED 455 nm LED 530 nm LED 660 nm LED 780 nm LED 1050 nm	0.072 0.042 0.036 0.241 0.075	59.4 64.7 71.0 50.3 32.7	This work

8. Technologies measurements (mechanical, solvent resistance and scalability)

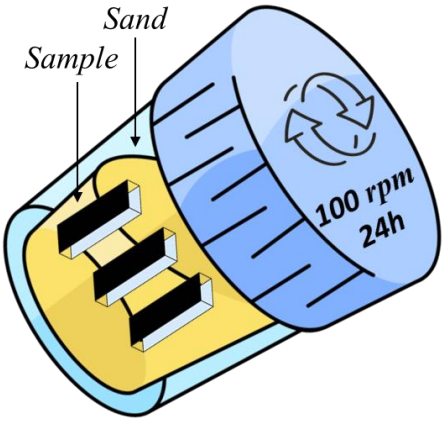

Fig. S15. Schematic illustration of the mechanical measurements.

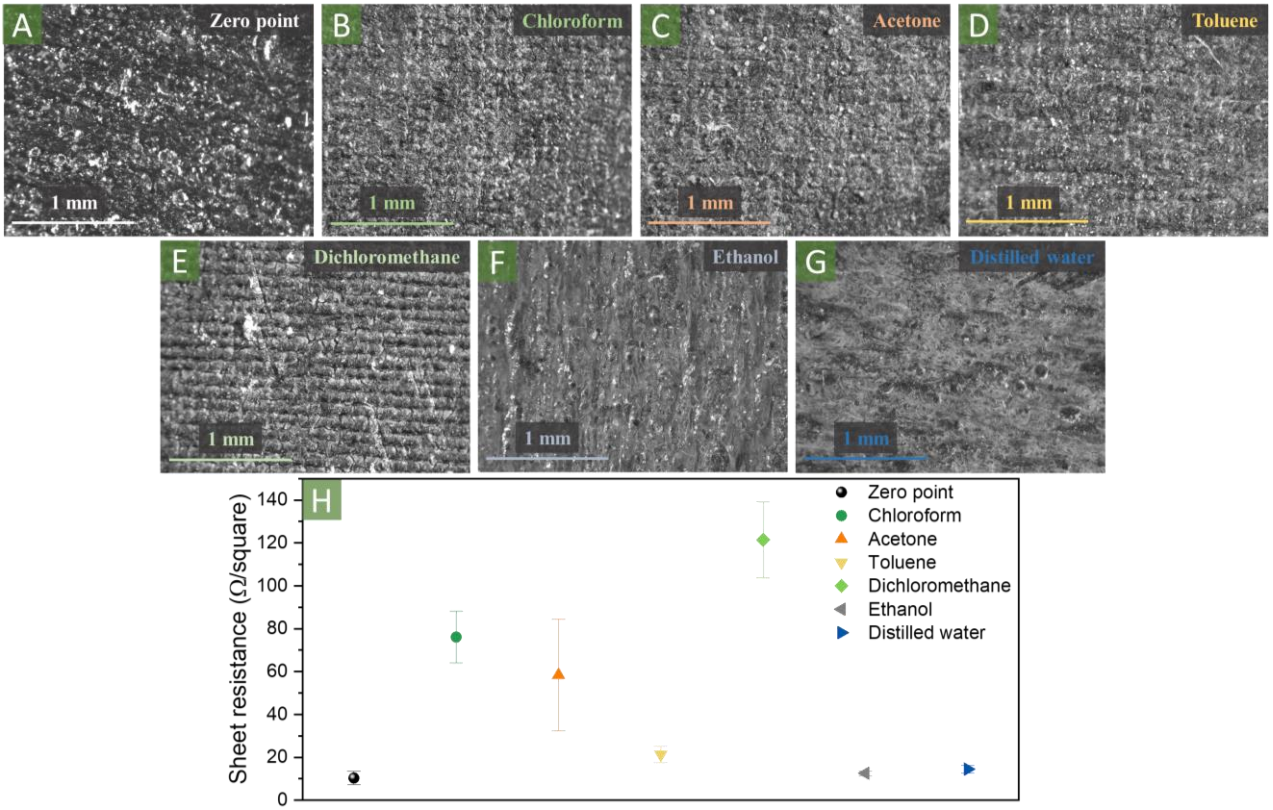

Fig. S16. Optical images (A) before and after soaking for 6 hours in: (B) chloroform, (C) acetone, (D) toluene, (E) dichloromethane, (F) ethanol, and (G) distilled water. (H) Resistance data before and after soaking for 6 hours in the same solvents.

Fig. S17. Five times enlarged graphitized PET@LB-UiO-66.

References

1 O. Semyonov, S. Chaemchuen, A. Ivanov, F. Verpoort, Z. Kolska, M. Syrtanov, V. Svorcik, M. S. Yusubov, O. Lyutakov, O. Guselnikova and P. S. Postnikov, *Appl. Mater. Today*, 2021, **22**, 100910.

2 X. Dyosiba, J. Ren, N. M. Musyoka, H. W. Langmi, M. Mathe and M. S. Onyango, *Sustain. Mater. Technol.*, 2016, **10**, 10–13.

3 C. O. Audu, H. G. T. Nguyen, C.-Y. Chang, M. J. Katz, L. Mao, O. K. Farha, J. T. Hupp and S. T. Nguyen, *Chem. Sci.*, 2016, **7**, 6492–6498.

4 J. Y. Seo, K. Y. Cho, J.-H. Lee, M. W. Lee and K.-Y. Baek, *ACS Appl. Mater. Interfaces*, 2020, **12**, 32778–32787.

5 F. Ahmadijokani, R. Mohammadkhani, S. Ahmadipouya, A. Shokrgozar, M. Rezakazemi, H. Molavi, T. M. Aminabhavi and M. Arjmand, *Chem. Eng. J.*, 2020, **399**, 125346.

6 Q. Zhao, W. Yuan, J. Liang and J. Li, *Int. J. Hydrogen Energy*, 2013, **38**, 13104–13109.

7 D. A. Sokolov, C. M. Rouleau, D. B. Geohegan and T. M. Orlando, *Carbon*, 2013, **53**, 81–89.

8 V. Strong, S. Dubin, M. F. El-Kady, A. Lech, Y. Wang, B. H. Weiller and R. B. Kaner, *ACS Nano*, 2012, **6**, 1395–1403.

9 E. Kymakis, K. Savva, M. M. Stylianakis, C. Fotakis and E. Stratakis, *Adv. Funct. Mater.*, 2013, **23**, 2742–2749.

10 J. Ren, C. Wang, X. Zhang, T. Carey, K. Chen, Y. Yin and F. Torrisi, *Carbon*, 2017, **111**, 622–630.

11 Y. C. Guan, Y. W. Fang, G. C. Lim, H. Y. Zheng and M. H. Hong, *Sci. Rep.*, 2016, **6**, 28913.

12 I. I. Bobrinetskiy, A. V. Emelianov, S. A. Smagulova, I. A. Komarov, N. Otero and P. M. Romero, *Mater. Lett.*, 2017, **187**, 20–23.

13 R. Rahimi, M. Ochoa, W. Yu and B. Ziaie, *ACS Appl. Mater. Interfaces*, 2015, **7**, 4463–4470.

14 A. R. Cardoso, A. C. Marques, L. Santos, A. F. Carvalho, F. M. Costa, R. Martins, M. G. F. Sales and E. Fortunato, *Biosens. Bioelectron.*, 2019, **124–125**, 167–175.

15 L. Cao, S. Zhu, B. Pan, X. Dai, W. Zhao, Y. Liu, W. Xie, Y. Kuang and X. Liu, *Carbon*, 2020, **163**, 85–94.

16 J. Edberg, R. Brooke, O. Hosseinaei, A. Fall, K. Wijeratne and M. Sandberg, *npj Flexible Electron.*, 2020, **4**, 17.

17 W. Zhang, R. Li, H. Zheng, J. Bao, Y. Tang and K. Zhou, *Adv. Funct. Mater.*, 2021, **31**, 2009057.

18 A. I. A. Soliman, A.-M. A. Abdel-Wahab and H. N. Abdelhamid, *RSC Adv.*, 2022, **12**,

7075–7084.

19 J. A. Bobb, A. A. Ibrahim and M. S. El-Shall, *ACS Appl. Nano Mater.*, 2018, **1**, 4852–4862.

20 M. Aleksandrzak, K. Sielicki and E. Mijowska, *RSC Adv.*, 2020, **10**, 4032–4039.

21 J. Geng, K. An, I.-N. Chan, H. Ai, K. H. Lo, K. W. Ng, Y. Kawazoe and H. Pan, *J. Mater. Chem. C*, 2021, **9**, 4748–4756.

22 N. R. Rathod, S. K. Gupta and P. K. Jha, *Solid State Commun.*, 2013, **169**, 32–36.

23 E. K. K. Abavare, S. N. A. Dodoo, K. Uchida, G. K. Nkurumah-Buandoh, A. Yaya and A. Oshiyama, *Phys. Stat. Solidi (b)*, 2016, **253**, 1177–1185.

24 K. Xue, L. Yan, Y. Ge, J. Zhang, R. Ku, Y.-M. Ding, Y. Jiao, Z. Zhu and L. Zhou, *Appl. Phys. Lett.*, 2022, **120**, 243101.

25 G. N. Abdelrasoul, B. Farkas, I. Romano, A. Diaspro and S. Beke, *Mater. Sci. Eng. C*, 2015, **56**, 305–310.

26 D. Bi, Y. Li, Y. Yao, T. Tao, B. Liang and S. Lu, *J. Alloys Compd.*, 2020, **825**, 153998.

27 H. Wang, Q. Dong, J. Yao, Z. Shao, J. Ma and X. Chen, *Biomacromolecules*, 2020, **21**, 1596–1603.

28 R. Li, L. Zhang, L. Shi and P. Wang, *ACS Nano*, 2017, **11**, 3752–3759.

29 X. Zhou, J. Li, C. Liu, F. Wang, H. Chen, C. Zhao, H. Sun and Z. Zhu, *Int. J. Energy Res.*, 2020, **44**, 9213–9221.

30 J. Liu, J. Yao, Y. Yuan, Q. Liu, W. Zhang, X. Zhang and J. Gu, *Adv. Sustain. Syst.*, 2020, **4**, 2000126.

31 W. Cai, Z. Li, Y. Pan, X. Feng, L. Han, T. Cui, Y. Hu and W. Hu, *J. Hazard. Mater.*, 2022, **437**, 129446.

32 C. Li, L. Li, J. Li, X. Wu, L. Qi and W. Li, *Cellulose*, 2019, **26**, 1631–1640.

33 Q. Yan, B. Xin, Z. Chen and Y. Liu, *Mater. Today Commun.*, 2021, **28**, 102584.

34 Q. Yan, B. Xin, Z. Chen and Y. Liu, *Mater. Today Commun*., 2021, **29**, 102877.